Additive manufacturing of an oxide ceramic by laser beam melting-Comparison between finite element simulation and experimental results

Liliana Moniz, Qiang Chen, Gildas Guillemot, Michel Bellet, Charles-André Gandin, Christophe Colin, Jean-Dominique Bartout, Marie-Hélène Berger

Additive manufacturing of an oxide ceramic by Laser Beam Melting – Comparison between finite element simulation and experimental results

Liliana MONIZ [(1)*], Qiang CHEN[(2)], Gildas GUILLEMOT[(2)], Michel BELLET[(2)], Charles-André GANDIN[(2)], Christophe COLIN[(1)], Jean-Dominique BARTOUT [(1)], Marie-Hélène BERGER[(1)]

MINES ParisTech, PSL Research University

1. MAT - Centre des matériaux, CNRS UMR 7633, 63-65 rue Henry Desbrueres BP 87, 91003 Evry Cedex, France
2. CEMEF – Centre de mise en forme des matériaux, CNRS UMR 7635, 1 rue Claude Daunesse, CS 10207, 06904 Sophia Antipolis Cedex, France

Abstract: Recent progress in the application of Laser Beam Melting (LBM) of oxide ceramics has shown promising results. However, a deeper understanding of the process is required to master and control the track development. In this approach numerical modeling could allow higher quality, of additive manufacturing for such materials, to be achieved. The validation of an earlier developed finite element model for LBM of ceramic materials has been established through a comparison with experimental results. The model solves heat and mass transfers whilst accounting for fluid flow due to surface tension and Marangoni convection, as well as tracking the material/gas boundary. The volumetric heat source parameters used in the simulations have been calibrated with an analytical model combined with original in-situ reflectance measurements. Numerical results show good agreement with measurements of melt pool dimensions and shapes. They also provide a coherent description of the evolution of the track morphology when varying the heat source parameters. Track irregularities have also been revealed by simulations at high scanning speed and the balling effect highlighted and explained through similar simulations.

Keywords: Laser beam melting; Ceramics; Simulation; Volumetric heat source; Reflectance; Melt pool stability

1. Introduction

Laser Beam Melting (LBM), also referred to as Selective Laser Melting (SLM), offers the possibility of producing parts with complex geometries and low porosity compared to other additive manufacturing (AM) technologies. Research mainly address metallic alloys with low forming capabilities when using conventional shaping technologies such as aluminum alloys (Olakanmi et al, 2015), stainless steel (Akita et al., 2016), titanium alloys (Liu et al., 2016; Schwab et al., 2016), cobalt-chromium (Averyanova et al., 2011) and nickel alloys (Harrison et al., 2015). However, despite their good mechanical strength and high thermal and wear resistances, few studies are available for ceramics. This could be due to their weak resistance to thermal shock and low absorption to near Infra-Red (IR) laser radiation experienced when using a Yb:YAG laser heat source. However, Hagedorn et al. (2010) reported that cracks can be avoided by preheating and Moniz et al. (2018) were able to overcome the low absorption of powders by adding a specific amount of IR-absorbers, such as carbon or silicon carbides particles.

Suitable and repetitive melt pool and track shapes are essential in LBM. They depend on the laser-matter interaction and the melt pool stability. The interaction between laser and ceramic powder is different from that of metals. Due to the low absorption of oxide ceramics, Yb:YAG laser radiation penetrates deeply into the ceramic material, acting as a volumetric heat source and leading to a much deeper melt pool. Addition of absorbers improves the material absorption and provides surface interaction with the heat source. It consequently affects the melt pool dimensions, which leads to the widening of a stable window for the manufacturing parameters. Optimal content is an intermediate value that helps maintaining powder bed integrity and melt pool stability through the limited quantity of absorbing sources. It should also be sufficient to absorb laser radiation. Melt pool stability is mainly controlled by fluid dynamics, in which surface tension, Marangoni convection and recoil pressure play

an important role. Absorption kinetics also affects the melt pool stability, when transferring the radiation absorbed to the ceramic particles. Under the effect of surface tension, high scanning speeds may result in the well-known balling effect. Li et al. (2012) experimentally observed that phenomenon for metals when processing a 316L stainless steel. The combined effects of Marangoni convection and recoil pressure were considered as sources of liquid spattering by Wang et al. (2017). The recoil pressure induced by evaporation has been seen to be partly responsible for powder denudation and a deleterious ejection of powder particles on the sides of the track, as shown by Moniz et al. (2018) and Matthews et al. (2016). As a result, the construction of repetitive regular tracks remains a principal difficulty due to the presence of these multiphysical phenomena influencing the track stability.

Numerical simulation helps to refine our understanding of the LBM process and provides guidelines to tailor the material and machine parameters to the targeted melt pool and track shape. For the melt pool shape, most studies have focused on the laser melting of dense material rather than a powder-bed. Li et al. (2012) investigated the heat transfer and melt pool shape for CO_2 laser melting of Al_2O_3 based ceramics. By solving the three-dimensional quasi-steady heat conduction equations, they compared a surface heat source model with the volumetric Beer-Lambert law for predicting the melt pool shape. The volumetric heat source was found to be more accurate and showed good agreement with melt pool depth and width. Li et al. (2004) then improved this model by taking into account latent heat and the heat convection, induced by Marangoni flow, applied to the $SiO_2 - Al_2O_3$ eutectic system. Good accuracy for melt pool profile was reported, also showing that latent heat has more influence than convection flow on the melt pool shape. A similar investigation by Yuan and Gu (2015) for $TiC/AlSi10Mg$ nanocomposite revealed the importance of Marangoni flow. It is noticeable that compared to metals, higher viscosity in ceramics may lessen the Marangoni effect. All mentioned results were obtained with continuum modelling approaches assuming a flat

surface and did not account precisely for LBM conditions. More precise investigations of the melt pool and track shape in laser or electron beam melting may be achieved with direct modeling of the powder particles (Körner et al., 2011; Khairallah and Anderson , 2014). As they need a complete description of the topology of the particles, such models are still computationally expensive and not commonly affordable.

There is little work dedicated to the numerical modeling of LBM applied to ceramics (Li et al., 2004 and 2012). Recently, the present authors Moniz et al. (2018) showed that the melt pool and track shape could be predicted while considering a continuous powder bed. A volumetric heat source based on the Beer-Lambert law was used, following the proposal of Li et al. (2012). The non-linear thermodynamic properties of the material, heat convection, surface tension and the related Marangoni effect were integrated as described by Chen et al. (2018). Although powder particles were not modeled in this approach, melt pool instabilities and track irregularities could be simulated and their origins were discussed.

The present work aims at comparing the simulated melt pool and track shape using the model developed by Chen et al. (2017) with experimental results produced by LBM of Al_2O_3 ceramic (Moniz et al., 2018). Dedicated experiments have been carried out with a specific powder-absorber mixture under different laser power and scanning speed, leading to different melted zones and track shapes. A set of relevant LBM experiments has been proposed in order to develop comparisons with an analytical model of melt pool shape and dimension. Mainly stable tracks were selected so as to develop this comparison leading to a first calibration of the volumetric heat source distribution and also to consider measurements of the reflection coefficient. Calibration of the numerical model has been achieved starting from this first set of parameters. Finally the simulation results have been compared with experiments, including melt pool profile, quantitative depth and width as well as with the track morphology. The influence of the scanning speed on the track shape regularity has then been

discussed with a special focus on the evaluation of the capability of the numerical simulation to detect and model the balling effect.

2. Experimental work

Experiments were carried out in a Phoenix PM100T LBM manufacturing machine. No shielding gas was required for the experiments so the ambient atmosphere was simply used. Alumina powder mixed with an IR-absorber was laid on a dense alumina substrate. Experiments were carried out with carbon graphite as the absorber. Before mixing with the absorber, the ceramic particles size at 50% of the cumulative distribution in volume (Dv_{50}) was 15 µm. Note that the addition of finer carbon black aggregates by Moniz et al. (2018) widened the size distribution and consequently affected the powder bed properties. Therefore, these alterations had to be taken into account when choosing a suitable absorber content. In the present study, a content of 1 wt.% carbon graphite was selected since it appeared to offer efficient energy absorption and reasonable melt pool stability.

The thickness of the deposited powder bed layer was measured to be equal to Δz_{powder} = 51 ± 7 µm. Its real porosity was estimated to be around 61.0 ± 0.5 % through profilometer analysis of in-situ depositions of the powder bed. Effective porosity was therefore no longer merely referred to as an interval between apparent and tapped densities as is usually the case.

Single tracks were melted using the near infra-red Yb:YAG laser radiation (1070 nm) supplied by the machine. The energy distribution of the laser beam was assumed to be described by a Gaussian law:

$$I(r) = (2P_L/\pi r_{\mathrm{L}}^2)\exp\ (-2r^2/r_{\mathrm{L}}^2) \qquad (1)$$

where I is the surface power, r is the radial coordinate through the beam transverse section, r_L is the nominal beam radius, and P_L is the nominal laser power. The surface power at $r = r_L$ is equal to the maximum surface power associated to the beam center ($2P_L/(\pi r_L^2)$) divided by the factor $e^2 \approx 7.4$. In the present experiments, the nominal laser radius was equal to $r_L = 35$ µm.

In order to accurately determine the heat source corresponding to the laser/material interaction, so as to develop numerical modeling, measurements of reflectance were carried out during the processing of single tracks to collect experimental variations of reflectance according to the set of processing parameters. Results are provided and discussed in Section 2.4.

A wide range of laser power, $\boldsymbol{P_L}$, and velocity, $\boldsymbol{v_L}$, was covered, corresponding to large variations of the nominal linear energy, $\boldsymbol{E_l = P_L/v_L}$. $\boldsymbol{P_L}$ and $\boldsymbol{v_L}$ parameters were varied regularly, respectively, within the interval [42, 168] W and [50, 800] mm·s^{-1}. $\boldsymbol{E_l}$ consequently covered the range [0.0525, 3.36] J·mm^{-1}. The following sub-sections present in detail the achieved experimental activity: characterization of melt pool width and depth by analysis of transverse sections of the tracks; study of the dispersion of tracks height and melt pool shape along the scanning direction. The definition of appropriate laser parameters for a stable process is reported below considering the analysis of these latter results. Finally, as already mentioned, a final sub-section presents laser reflectance measurements and the set of material properties to be used in process numerical simulation.

Note that further comparison using thermal imaging could complete the experimental data. However, dynamic imaging of oxide ceramics is limited due to the semi-transparency of these materials in the near-IR as pointed out by Carillon (2007). Information collected with

traditional near-IR thermal imaging would therefore give access to the whole volume information underneath and not only at the surface of the material, as it is the case for metals.

2.1. Tracks aspect and stability

Top views of the tracks obtained when varying power and speed of the laser for the set of investigated process parameters are shown in Figure 1. As expected, the figure reveals the widening of the track with increase of laser power and the decrease of scanning speed. Track irregularities appeared to be more frequent and marked at high speed. Spikes on the both sides of the tracks could be observed in most cases. These irregularities may have been related to the stochastic distribution and size of IR-absorbers and the ceramic particles themselves. Spikes can also be favored by substrate cracking caused by high tensile stresses, mainly at high laser power. An additional phenomenon contributing to track irregularity was powder denudation, which appeared at high speed. Periodical transverse cracks could also be observed, essentially for tests performed at high linear energy. They were caused by tensile stresses exerted in the direction of the laser scanning. Such cracks are different from solidification cracks, which form in the mushy state, at the rear of the molten pool, with a cracking plane containing the local temperature gradient vector. Here it can be presumed that the cracks observed formed after complete solidification, during the cooling of the track. Each crack formation was associated with stress relaxation in the neighborhood, which explains the quasi periodical regime observed. As proposed by Hagedorn et al. (2010), such a phenomenon could be hopefully eliminated by using an auxiliary laser with a defocused beam, having the role of controlling the cooling of the track in the wake of the melt pool.

Track stability is definitely of paramount importance for additive manufacturing and sound construction of components. Consequently the eight better processing conditions, highlighted by bold outlines in Figure 1, were be retained for the rest of the study, and as a support for further comparisons with numerical modeling.

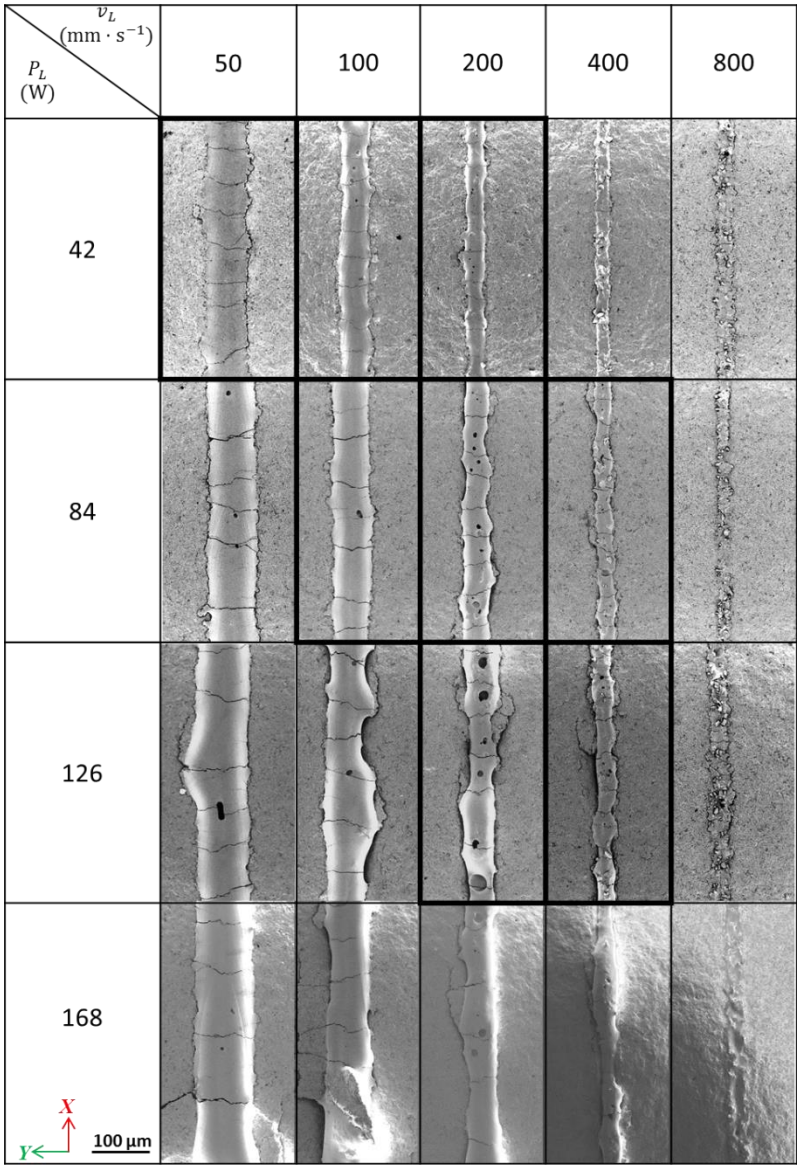

Figure 1: Top views of tracks obtained under different process conditions (nominal laser power P_L (W) and scanning speeds v_L (mm · s^{-1})). Linear energy domain extended from 0.0525 up to 3.36 J · mm^{-1}. Bold outlines indicate tracks selected for numerical comparison in Section 4.

2.2. Melt pool dimensions

The melt pool was characterized by its height, H_{pool}, and its width, w_{app} measured in a transverse cross section, as illustrated in Figure 2. The upper consolidated part was associated with its height, H_{app}, and its area, S_{app}. The lower remelted area of the track was

characterized by its depth, H_{ZR}, and its section, S_{ZR}. Experimental uncertainty, due to the measurement methodology, was evaluated as ± 5 µm . The contour of the remelted region was identified mainly by the presence of cracks at the boundary with the substrate. This limit has also been confirmed through a change in microstructure as revealed in Figure 3. The substrate was produced by powder sintering and characterized by an equiaxed grain structure. Conversely, a dendritic columnar microstructure was observed as a result of melt pool solidification oriented along the temperature gradient. Note that the limit between melt pool and substrate, shown in Figure 2, is rather obvious, but identifying the "last bath" boundary (along a longitudinal transversal cut section when the laser was switched off) in the remelted region was not as explicit as for metallic systems. The reason is linked to the difference in internal microstructure that was not clearly revealed for the almost pure alumina, i.e. a material with little imaging contrast due to segregation of species. In the case of metallic alloys, the "last bath" boundary is identified by a clear difference in the grain size and its internal microstructure that is mainly revealed by segregation. Note also that spherical porosities caused by gas entrapment after complete solidification could sometimes be observed in the consolidated track material. All melt pool sections obtained in different process conditions will be presented below when compared with numerical simulations.

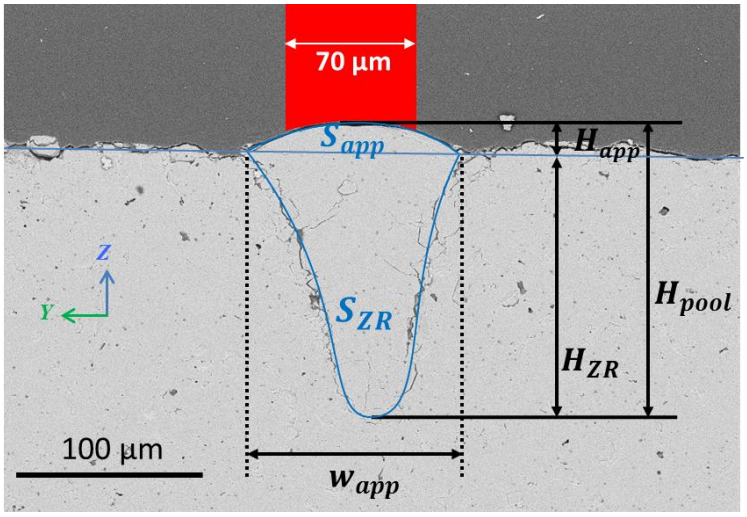

Figure 2: Definition of characteristic melt pool dimensions: lengths (H) and areas (S). Present results were obtained for process parameters $P_L = 42$ W and $v_L = 100$ mm · s^{-1} briefly referred as $P_L 42 v_L 100$.

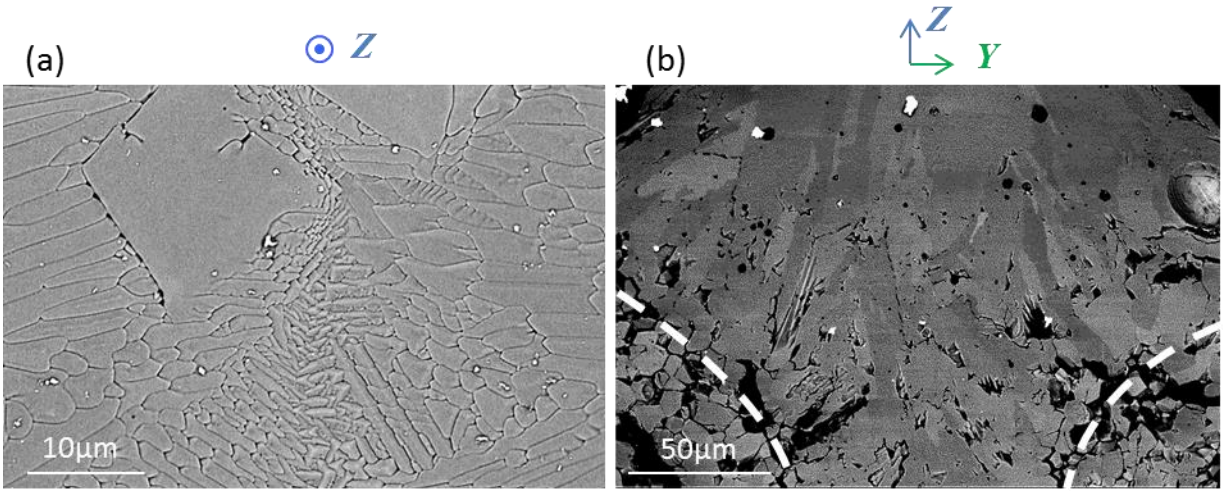

Figure 3: Microstructure observed by scanning electron microscopy after melt pool solidification: (a) columnar dendrites (top view) and (b) grains with approximate substrate limits identified by white dashed lines (transverse section view). The vector ***Z*** (Figure 2) indicates the building direction.

Along each track, the height value, H_{app}, varied significantly in unstable conditions. Thus, H_{app} was measured along each track using optical profilometry and an average value calculated for each track. The width w_{app} has been averaged by several top view measurements along the tracks as presented in Figure 1. The depth H_{ZR} was characterized by only a single transverse cut per track. Several longitudinal cuts views developed for a given

choice of process parameters showed that the H_{ZR} variations were negligible for a given scan. Consequently, the variations of H_{ZR} for a given set of process parameters have not been considered in the present estimations

A suitable melt pool shape for additive manufacturing is characterized by a small number of remelted layers, this number being approached by the ratio H_{ZR}/H_{app}, and by a low aspect ratio, H_{pool}/w_{app}. According to the experience of the authors, no more than 6 layers should be remelted for ceramic materials in order to get a good cohesion with the previous melted layers whilst allowing for the removal of gaseous entrapments (porosities) from the melt pool. On the other hand, appropriate values for the aspect ratio should lie between 0.5 and 2.5. It is important again to notice that for IR-absorbing materials, such as metals, these values are smaller. This is due to the penetration depth of laser radiation being limited in the latter case, except when the keyhole mode was activated. Measured values are presented in Figure 4 and Table 1. Well-suited working conditions corresponding to the two domains proposed previously for remelted layers (H_{ZR}/H_{app}) and aspect ratio (H_{pool}/w_{app}) would not exceed 1 J·mm^{-1} linear energy according to average tendencies plotted (power laws fit). Tracks at high power where not used for numerical comparison since they are too energetic when studying 2D juxtaposed tracks (varying hatch spacing). Melting of a mixed environment composed by the previous melted track without an absorber and the powder bed mixture (ceramic and absorber) explain the differences between stability of 1D tracks and 2D juxtaposed tracks.

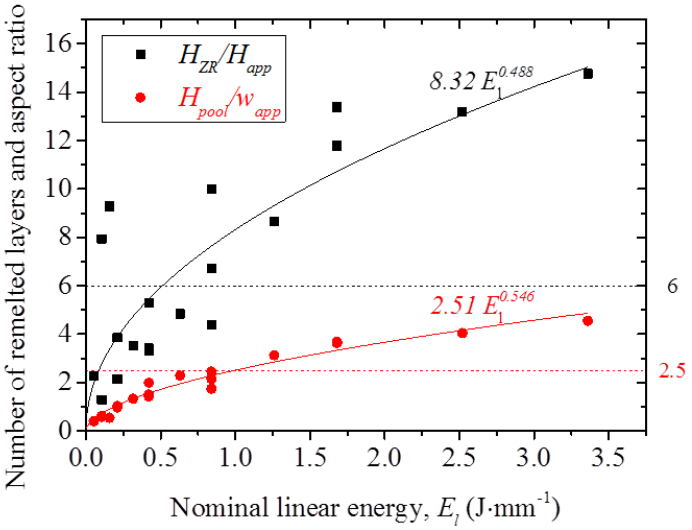

Figure 4: Number of remelted layers (H_{ZR}/H_{app}), and pool aspect ratio (H_{pool}/w_{app}) as a function of the nominal linear energy E_l. Threshold values suitable for manufacturing are also highlighted. Average tendencies can be properly fitted with power laws.

	E_l (J · mm^{-1}) H_{ZR}/H_{app} H_{pool}/w_{app}				
P_L (W) \ v_L (mm · s^{-1})	50	100	200	400	800
42	0.84 *10.0* **1.7**	0.42 **5.3** **1.5**	0.21 **2.1** **1.0**	0.11 **1.3** **0.6**	0.05 **2.3** *0.4*
84	1.68 *13.4* *3.6*	0.84 *6.7* **2.4**	0.42 **3.3** **2.0**	0.21 **3.9** **1.0**	0.11 *7.9* **0.6**
126	2.52 *13.2* *4.0*	1.26 *8.7* *3.1*	0.63 **4.8** **2.3**	0.32 **3.5** **1.3**	0.16 *9.3* ***0.5***
168	3.36 *14.8* *4.5*	1.68 *11.8* *3.7*	0.84 **4.4** **2.1**	0.42 **3.4** **1.4**	0.21 *50.6* *0.5*

Table 1: Linear energy,E_L, number of remelted layers, H_{ZR}/H_{app}, and pool aspect ratio, H_{pool}/w_{app}, for all (P_L, v_L) conditions, corresponding to Figure 4. Values considered suitable for additive manufacturing are highlighted in bold and bold outlines indicate tracks selected for numerical comparison in Section 4.

2.3. Stability criteria

Several types of track morphologies could be identified related to the linear energy employed. Below a minimal linear energy value, $E_{l\,min}$, melting was not continuous and no track was created. When progressively increasing the linear energy, the pool morphology progressively changed from an "elliptical" shape, $H_{pool} < w_{app}$, at low linear energies (domain labeled E in Figure 5), to a "triangular" shape, $H_{pool} > w_{app}$, at medium linear energies (domain labeled T in Figure 5). The linear energy at which H_{pool} and w_{app} were equal, *i.e.* for which the aspect ratio H_{pool}/w_{app} reached unity, is defined by $E_l^{E-T} = E_l(H_{pool} = w_{app})$. High linear energies, usually over 1 J·mm^{-1}, were related to the keyhole domain (labeled K in Figure 5). Melt pools were then very deep and unstable, leading to a high fraction of porosity and stresses upon solidification and thus unsuitable for manufacturing processes. We denote E_l^{T-K} as the transition value between triangular and keyhole modes. According to the previous geometrical criteria of aspect ratio and number of remelted layers, most stable morphologies were obtained for linear energies near E_l^{E-T}, either in the elliptical or triangular regions.

The variation of height along each track, D, is defined by the ratio of standard deviation, σ to the mean average height, $\overline{H}_{app}$:

$$D = \sigma/\overline{H}_{app} \quad (2)$$

Track steadiness was characterized by low dispersion values, typically less than 50%. A stability map presenting D variations as a function of laser power and scanning speed is proposed in Figure 5. Critical transition linear energies E_l^{E-T} and E_l^{T-K} are also sketched in

this stability map. Highest D values were obtained at high laser speed. However, they were also found in the domain corresponding to the elliptical regime for high values of laser power. In total, most appropriate process parameters, combining low D values and acceptable melt pool dimensions, were chosen for the experimental-numerical comparison. These selected process conditions are shown as black dots in Figure 5. The corresponding linear energies range from 0.21 to 0.84 J·mm^{-1}. The selected laser parameters are listed in Table 2.

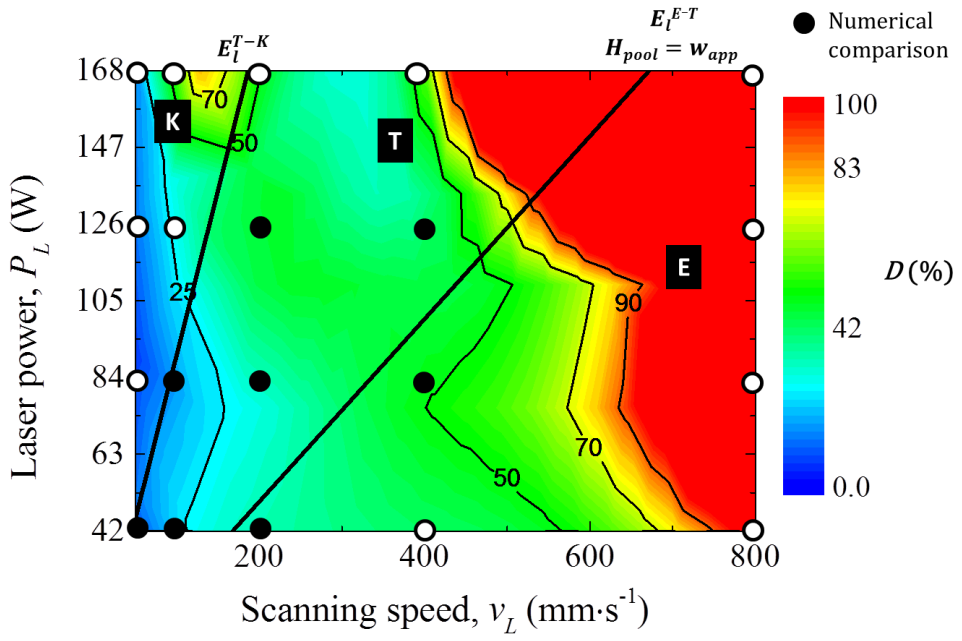

Figure 5: Stability map showing the distribution of height variation, D, as a function of the laser power, P_L, and velocity, v_L. Domains of different melt pool features are labeled: (T) triangular shape, (E) elliptical shape, and (K) keyhole regime. The transition limits between elliptical and triangular melt pool, E_l^{E-T}, and between triangular melt pool and the occurrence of keyhole, E_l^{T-K}, are sketched with black straight lines. Black and white dots correspond to experimental conditions studied, the black ones were chosen for numerical comparisons (see bold outlines in Figure 1 and Table 2).

Case number #	**1**	**2**	**3**	**4**	**5**	**6**	**7**	**8**
$\boldsymbol{P_L}$ **(W)**	42	42	42	84	84	84	126	126
$\boldsymbol{v_L}$ **(mm** $\cdot$ $\mathbf{s^{-1}}$**)**	50	100	200	100	200	400	200	400
$\boldsymbol{E_l = P_L/v_L}$ **(J** $\cdot$ $\mathbf{mm^{-1}}$**)**	0.84	0.42	0.21	0.84	0.42	0.21	0.63	0.315

Table 2: Laser parameters (P_L, v_L) providing track stability and chosen for comparisons between numerical simulations and experiments (see bold outlines in Figure 1 and black dots in Figure 5).

2.4. Material properties and reflectance measurements

This section focuses on the material properties required in view of the numerical simulation of the process which will be reported in Section 3. The material properties are provided in Table 3. Note first that alumina has a high melting point ($T_m = 2054$ °C). In the context of this study, taking into account the numerical difficulty of releasing the latent heat at a fixed temperature, a solidification interval of arbitrary amplitude [2004, 2104] °C was considered. Note that due to the strong temperature gradient found during LBM, the dimension of the region where latent heat was released remained very small compared to the melt pool. The high viscosity of liquid alumina should also be mentioned, typically one order of magnitude higher than for liquid metals. This leads to damped fluid dynamics in the liquid pool. The Marangoni effect has been taken into account by assuming a linear temperature dependency of the surface tension coefficient.

	Property	Symbol	Value	Unit	Reference
Al_2O_3	Density	ρ^a	3970	kg·m^{-3}	(Aksay et al., 1979)
	Specific enthalpy	h^a	Fig. 5(a) in (Chen et al., 2017)	J·kg^{-1}	(Chase, 1998)
	Fusion enthalpy	$\Delta h_{v,f}$	1.252×10^{10}	J·m^{-3}	(Chase, 1998)
	Thermal conductivity	λ^a	$5.5 + 34.5\exp(-0.0033\,T)$ with $T \in [25, 1300]$ °C	W·m^{-1}·K^{-1}	(Touloukian et al., 1984)
	Liquid viscosity	μ^a	$2.15 \cdot 10^{-3} \exp\left(\frac{57685}{R_g T}\right)$ for $T \in [2327, 3243]$ K	Pa·s	(Langstaff et al., 2013)
	Melting point	T_m	2054	°C	(Chase, 1998)
	Solidification interval (artificial)		2004 - 2104	°C	(Chen et al., 2017)
Gas (air)	Density	ρ^g	1.3	kg·m^{-3}	"Dry air properties", 2017
	Specific heat	C_p^g	1000	J·kg^{-1}·K^{-1}	
	Thermal conductivity	λ^g	0.024	W·m^{-1}·K^{-1}	
	Viscosity	μ^g	$2.4 \cdot 10^{-5}$	Pa·s	
Liquid Al_2O_3/Gas	Surface tension	γ	$0.64 - 8.2 \cdot 10^{-5}(T - 2327)$ for $T \in [2190, 2500]$ K	N·m^{-1}	(Paradis and Ishikawa, 2005)

Table 3: Physical properties of alumina and gas.

For numerical modeling, the knowledge of reflectance factor values, R, is essential. Indeed, this parameter also characterizes the amount of nominal laser power entering the material. However, literature does not supply an evaluation of this value. Consequently operando measurements were carried out inside the machine during laser manufacturing. The spectral hemispherical signal was collected through an integrating sphere (RT-060 from Labsphere®) for all P_L and v_L conditions listed in Table 1. Figure 6 describes how in-situ measurements were acquired. After the usual deposition of the powder bed on the dense substrate, the sample was inclined by an angle of 10° in order to confine the specular

reflection (of the melted material) inside the integrating sphere. Calibration had been undertaken beforehand with a 100% reflectance sample provided by Labsphere®. Then the signal emitted from the studied sample was continuously recorded for each track, before and during material melting, as well as after solidification. Note that incident laser radiation was suppressed via a band cut filter at 1070 nm.

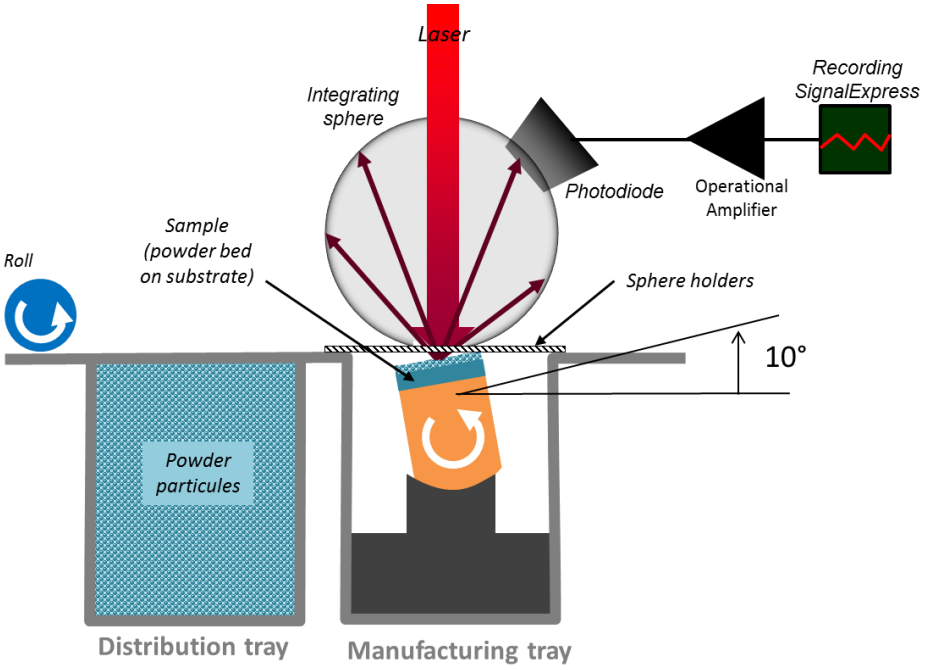

Figure 6: Set up for spectral hemispherical reflectance measurements

Results presented in Figure 7 show the variation of the reflectance R when increasing the linear energy E_l. The R value is indeed a function of process parameters and was found to decrease with E_l. High dispersion values of R for some values of E_l could be explained by different values in P_L or v_L providing the same E_l value. Despite this variation, it was remarkable that a decreasing power law was quite reasonable in describing the R evolution. A similar trend was observed by direct calorimetric measurements y Trapp et al. (2017). These first dynamic measurements, completed with alternative static acquisitions, indicated that, at low linear energy (high scanning speed), the laser spot was mostly located on the powder bed, so that the R value approached the powder bed value. Conversely, at high linear energy (low

scanning speed), the laser spot was mostly located on the liquid pool, so that the R value was closer to the liquid material value. These aspects have already been discussed by Gusarov and Smurov (2010) and Gunenthiram et al. (2017).

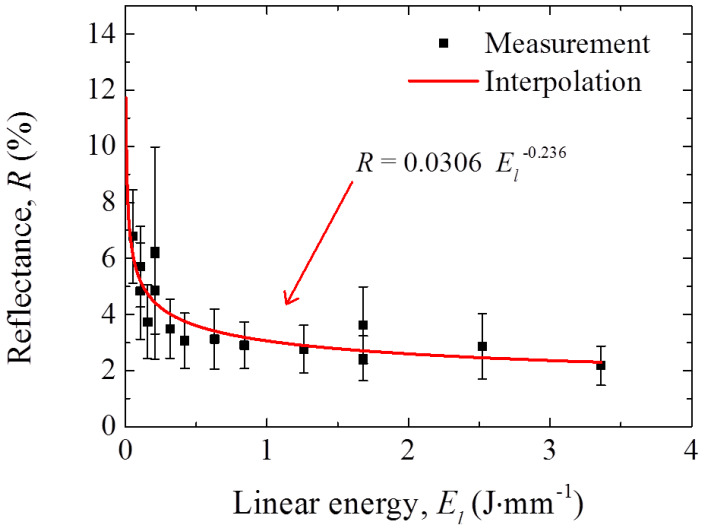

Figure 7: Spectral hemispherical reflectance obtained by in-situ optical measurement.

3. Modeling and simulation

3.1. Presentation of the finite element model

A numerical finite element model applied at the scale of few single tracks has been developed for the simulation of LBM applied to ceramics (Chen et al., 2017). Two domains have been considered, namely the gas and the material. The material was that of the substrate, plus the consolidated material (tracks), and finally the powder bed. The latter was thus assimilated to a continuum with homogenized (apparent) properties. The level set (LS) method was used to follow the temporal and spatial evolution of the gas/material interface caused by the fusion of the powder bed, the melt pool dynamics, and the powder consolidation. The change of the apparent density of the powder bed transforming into dense

alumina due to melting and solidification was thus accounted for. Both heat transfer and liquid flow were simulated in this two-domain system. Only the essential features of the numerical model are presented below, more details being available in the literature (Chen et al., 2017 and 2018). Note that the model does not account for the keyhole phenomenon as this regime is not suitable for a stable additive construction.

The transient heat transfer equation taking into account convection and diffusion phenomena is expressed as follows:

$$\frac{\partial\{\rho h\}}{\partial t} + \nabla \cdot (\{\rho h\}\boldsymbol{u}) - \nabla \cdot (\{\lambda\}\nabla T) = \dot{q}_L - \dot{q}_r \qquad (3)$$

where curl brackets stand for the mixture of quantities operated around the material/gas interface, namely the volumetric enthalpy, ρh, and the thermal conductivity, λ. The convection velocity,$\boldsymbol{u}$, is the solution of the Navier-Stokes equation presented later. The right hand side quantities $\dot{q}_L$ and $\dot{q}_r$ are the laser heat input and the heat loss by radiation along the material/gas interface, respectively. The phase transformation path is coupled with this non-linear equation. It takes into account the powder bed fusion and its re-solidification as a compact track, including the latent heat of the transformations. However, the liquid-gas transformation (evaporation) has not been taken into account in the present study.

An important term in Eq. (3) is the heat source $\dot{q}_L$. The laser radiation reaching the material surface was partially reflected according to the value of the medium reflection coefficient *R* as estimated in Figure 7. The penetrating flux was then attenuated in the quasi-transparent material according to the Beer-Lambert law (Chen et al., 2018). In the case of a granular material such as a powder bed, multiple reflections occur on the particle surfaces according to Fischer et al. (2003). By contrast with the laser interaction with a dense material, this phenomenon leads to a larger region affected by laser radiation. In order to take into

account this effect, it is assumed that the interaction radius, r_{int}, is greater than the nominal laser radius, r_L, whilst the laser flux kept the form of a Gaussian distribution. The volumetric heat source $\dot{q}_L$ was then based on the Beer-Lambert law, written as:

$$\dot{q}_L = (1 - R)\,\frac{2P_L}{\pi r_{int}^2}\exp\left(-\frac{2r^2}{r_{int}^2}\right)\,\alpha\,\exp\left(-\int_0^z \alpha\, dl\right) \qquad (4)$$

where r is the distance to the laser axis and z is the distance below the material/gas interface, in the (vertical) direction of the laser beam. The absorption coefficient α appears in the integral term as the attenuation of the laser intensity during propagation into the material. Note that α is dependent on the material state as solid, α_s, liquid, α_l, and powder bed, α_p may have different absorptions values.

The melt pool dynamics have been modeled by the momentum conservation equation (Navier-Stokes equation):

$$\{\rho\}\left(\frac{\partial \boldsymbol{u}}{\partial t} + (\boldsymbol{u}\cdot\nabla)\boldsymbol{u}\right) - \nabla\cdot\left\{\underline{\underline{\boldsymbol{\sigma}}}\right\} = \boldsymbol{f}_V \qquad (5)$$

where $\underline{\underline{\boldsymbol{\sigma}}}$ is the stress tensor and $\boldsymbol{f}_V$ is the volumetric driving force, including surface tension, Marangoni force and gravity (Chen et al., 2018). The stress tensor is related to the strain-rate tensor and consequently to the velocity field, $\boldsymbol{u}$, by the Newtonian behavior law with the viscosity μ. Eq. (5) coupled with the mass conservation equation (Chen et al., 2017) :

$$\nabla\cdot\boldsymbol{u} = \dot{\theta} \qquad (6)$$

where $\dot{\theta}$ denotes the volume contraction rate associated with the condensation from powder to dense matter in the context of a continuous powder bed. The velocity field $\boldsymbol{u}$ is used to update the material/gas interface by the LS function ψ using the transport equation:

$$\frac{\partial \psi}{\partial t} + \boldsymbol{u} \cdot \nabla \psi = 0 \quad (7)$$

However, transport of ψ does not guarantee the Eikonal property, $\|\boldsymbol{\nabla}\psi\| = 1$. Hence, ψ has been recomputed by a geometrical method with respect to the position $\psi = 0$ which was obtained by the resolution of Eq. (7) (Chen et al., 2017).

3.2. Analytical model for a first order estimation of melt pool size

An analytical model was established by Defillon et al. (2014) to predict the melt pool size. In this simplified two-dimensional model, heat exchange by conduction or convection was not considered. Material absorption was distinguished between liquid and non-liquid (*i.e.* $\alpha_s = \alpha_p$), with absorption coefficients α_l and α_s, respectively. The model assumed that the increase of volumetric enthalpy Δh_v of the material should be equal to the fusion enthalpy $\Delta h_{v,f}$ in order to be melted. Considering an arbitrary point at coordinates (x, y, z), the total volumetric energy absorbed by this point when the laser moves in the x-direction could be calculated by time-integration of the volumetric heat source defined by Eq. (4). In the transverse section (yz plane), the melt pool boundary is expressed as:

$$z_l(y) = \frac{1}{\alpha_l} \ln\left(1 + \alpha_l \left[\sqrt{\frac{2}{\pi}} \frac{(1-R)E_l}{r_{int}\Delta h_{v,f}} \exp\left(-\frac{2y^2}{r_{int}^2}\right) - \frac{1}{\alpha_s}\right]\right) \quad (8)$$

when the following fusion condition is satisfied:

$$E_l \geq E_{l\,min} = \sqrt{\frac{\pi}{2}} \frac{\Delta h_{v,f} r_{int}}{\alpha_s (1-R)} \quad (9)$$

Eq. (8) gives the full description of the melt pool shape. In particular, it gives access to the melt pool width by considering that z_l should be zero for $y = w_{app}/2$. This simply yields:

$$w_{app}^2 = 2r_{int}^2 \ln(E_l / E_{l\,min}) \quad (10)$$

In addition, by taking, $y = 0$, the melt pool depth can also be deduced:

$$H_{ZR} = z_l(0) = \frac{1}{\alpha_l} \ln\left(1 + \frac{\alpha_l}{\alpha_s}\left[\frac{E_l}{E_{l\,min}} - 1\right]\right) \quad (11)$$

It should be noted that this analytical solution can only provide a first rough estimation of the melt pool shape, due to the limitations of assumptions and hypotheses previously detailed. With the presence of convection and conduction, the melt pool shape is expected to be different from this analytical prediction. The numerical finite element – level set model introduced in Section 3.1 has been used to obtain refined estimations of the shape of the fusion zone.

3.3. Volumetric heat source parameters

The volumetric heat source parameters in Eq. (4), particularly the effective interaction radius r_{int} and the absorption coefficients of the material, α_s and α_l, are difficult to measure. Although α-values are reported by Lawrence (2004) and Bityukov and Petrov (2013), variations can extend over several orders of magnitude. Alumina shows low absorption of Yb:YAG laser light, and it can be strongly modified by impurities. It is thus proposed to first calibrate these 3 parameters with the help of measurement of the melt pool size and by the use of the analytical model. In order to find these 3 heat source parameters, it is proposed to minimize the following total error function:

$$(r_{int}, \alpha_s, \alpha_l) = \underset{(r_{int},\alpha_s,\alpha_l)}{\arg\min} \sum_{(P_L^i, v_L^i) \in G} \left[\left(\frac{H_{ZR}^{i,ana}}{H_{ZR}^{i,exp}} - 1 \right)^2 + \left(\frac{w_{app}^{i,ana}}{w_{app}^{i,exp}} - 1 \right)^2 \right] \quad (12)$$

where the superscripts ana and exp denote the analytical solution and experimental results, respectively. The set G is the ensemble of the eight selected processing conditions listed in Table 2. With the experimental data, the 3 heat source parameters have been firstly estimated by Eq. (12) in Section 4.1. Then the obtained parameters will be adjusted in Section 4.2.

3.4. Simulation configuration

The whole simulated system is shown in Figure 8 with overall dimensions; $3 \times 0.5 \times 1.1\ \mathrm{mm}^3$. Gas (at top, transparent 0.1 mm-thick layer) and material (including powder and substrate) were separated by the LS interface initially at $z = 1$ mm. A layer of powder with thickness 51 μm and porosity of 61% was deposited on the substrate. A laser beam linearly scanned the powder from the top with initial position (x, y) = (0.2, 0.25) mm and final position (2.8, 0.25) mm, i.e. in the median plane. The laser velocity was kept constant. While the laser is turned on at time $t = 0\ s$ and off when it reached the final position, the simulations continued until all liquid was solidified. As shown in Figure 8, the simulation could provide access to the temperature distribution, the melt pool shape and the track shape.

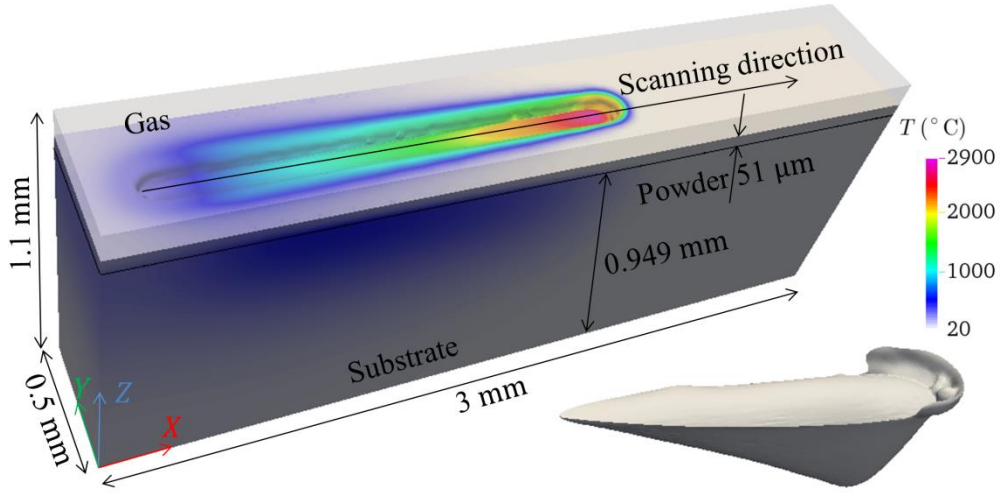

Figure 8: Dimensions of the simulated system with temperature field and 3D melt pool shape obtained in the case $P_L 84 v_L 200$. The total simulated time was 13 ms till complete solidification..

The initial and ambient temperatures were set to be 20 °C. For the thermal resolution, the top boundary of the simulation domain was adiabatic and heat flux through the other faces was defined by a heat transfer coefficient of 40 $\mathrm{W \cdot m^{-2} \cdot K^{-1}}$ and an outside temperature of 20 °C. For the resolution of melt pool dynamics, a pure sliding condition has been considered along the four lateral faces; a sticking condition was imposed along the lower face; the upper face was free. Anisotropic mesh adaptation was used, based on an error estimation method. The number of elements evolved from ~1 200 000 at the beginning of the simulation to ~1 430 000 at the end of the simulation in order to keep a good topological representation of the track shape and an appropriate mesh refinement along the boundaries of the melt pool (see details in (Chen et al. 2017 and 2018)).

4. Identification of parameters: results and discussion

4.1. First identification using the analytical model

The minimization of Eq. (12)(12), using the analytical model based on Eq. (8) - Eq.(11), led to $r_{int,1} = 73.1\ \mu m$, $\alpha_{s,1} = 8.13\ mm^{-1}$, and $\alpha_{l,1} = 6.1\ mm^{-1}$. Comments on these values are expressed below, at the end of Section 4. These heat source parameters were then used in the finite element simulations for the different process conditions listed in Table 2. Measured melt pool width and depth are shown in Figure 9 as a function of the scanning speed for different values of the laser power, together with the analytical and numerical predictions. The substrate was found not to be molten in the material domain in $P_L 42 v_L 200$. Note that, according to Eqs. (10) and (11), the melt pool size predicted by the analytical model only depended on the linear energy E_l. Therefore, the same melt pool size was predicted for cases $P_L = 42\ W$, $v_L = 100\ mm \cdot s^{-1}$ (denoted in short $P_L 42 v_L 100$) and $P_L = 84\ W$, $v_L = 200\ mm \cdot s^{-1}$ ($P_L 84 v_L 200$). However, this is not in agreement with measurements.

The above set of three parameters has been used in the finite element simulation of the different process conditions. The results are labeled "Simulation" in Figure 9. Significant differences have been observed between the analytical prediction and numerical simulation, especially for the melt pool depth. All H_{ZR} values obtained by numerical simulations were lower than those of analytical predictions and experimental measurements. It should also be noted that according to the finite element model, the substrate was found not to be molten in case $P_L 42 v_L 200$. These differences were mainly due to the effect of conduction, convection, and also the presence of the powder layer in the numerical simulation, the analytical model being based on the sole dense substrate, without conduction and convection.

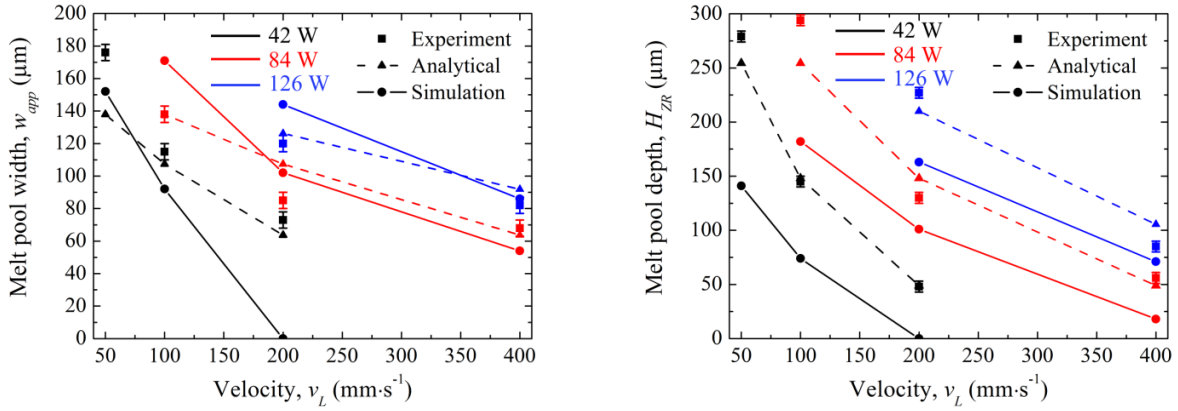

Figure 9: Melt pool (a) width, w_{app}, and (b) depth, H_{ZR}, as a function of the laser velocity, v_L, for laser power (black) 42 W, (red) 84 W and (blue) 126 W (Table 2). Note that the indicated error interval is limited since it is representative of the measurement error for one transversal cut, and not for several cuts along one track. Comparison is provided between experiments, analytical solutions and finite element simulations with heat source parameters firstly deduced by Eq. (12): $r_{int,1} = 73.1$ µm, $\alpha_{s,1} = 8.13$ mm^{-1}, and $\alpha_{l,1} = 6.1$ mm^{-1}.

4.2. Second identification with the numerical model

Considering the differences between the analytical model and the finite element simulation, it was proposed to correct the first estimation of parameters$(r_{int,1},\ \alpha_{s,1},\ \alpha_{l,1})$. Actually, it may be supposed that the difference between analytical and simulation for the melt pool dimensions remained almost unchanged under certain process conditions when the heat source parameters were slightly changed. Hence, the minimization function was modified as follows to determine a second set of parameters:

$$(r_{int}, \alpha_s, \alpha_l) = \underset{(r_{int},\alpha_s,\alpha_l)}{\arg\min} \sum_{(P_L^i, v_L^i)\in G} \left[\left(\frac{H_{ZR}^{i,ana} - \Delta H_{ZR,1}^i}{H_{ZR}^{i,exp}} - 1 \right)^2 + \left(\frac{w_{app}^{i,ana} - \Delta w_{app,1}^i}{w_{app}^{i,exp}} - 1 \right)^2 \right] \qquad (13)$$

where depth and width differences were calculated for each i-parameter (P_L^i, v_L^i) from the data of the first calibration shown in Figure 9:

$$\Delta H_{ZR,1}^{i} = H_{ZR,1}^{i,ana} - H_{ZR,1}^{i,sim} \quad \text{and} \quad \Delta w_{app,1}^{i} = w_{app,1}^{i,ana} - w_{app,1}^{i,sim} . \qquad (14)$$

Solving Eq. (13) led to the following modified values: $r_{int,2} = 64.6$ µm , $\alpha_{s,2} = 8.98\ \text{mm}^{-1}$ and $\alpha_{l,2} = 3.88\ \text{mm}^{-1}$. These parameters were then used in the finite element model simulation to compare the melt pool shape with experimental measurements.

A quantitative comparison of melt pool width and depth with the new set of parameters is given in Figure 10. Compared with the first simulation results in Figure 9, heat source parameters deduced with correction using Eq. (13) resulted in a much better agreement between experiments and numerical simulations. Among them, cases P_L84v_L20, P_L84v_L400, P_L126v_L200 and P_L126v_L400 matched closely the experiments for both width and depth. The principal differences were found for cases with the lowest power, $P_L = 42$ W, for which the melt pool obtained by the numerical simulation was smaller than in experiments, both in width and depth. The procedure of parameter calibration might be performed again to further minimize the difference. However, excellent fitting was still difficult due to the complexity of the interaction between laser and material, especially in the powder and with the presence of carbon absorbers. The absorption distribution must have been much more complicated than that assumed between the liquid and the non-liquid material as simplified in the model.

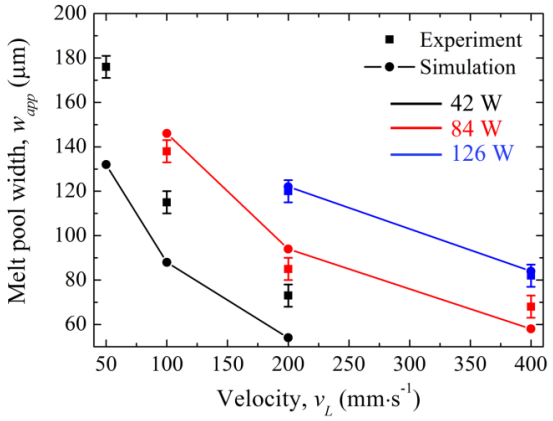

(a)

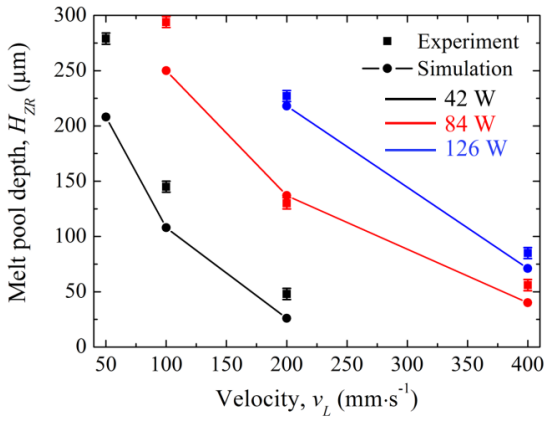

(b)

Figure 10: Melt pool (a) width, w_{app}, and (b) depth, H_{ZR}, as a function of the laser velocity, v_L, for laser power (black) 42 W, (red) 84 W and (blue) 126 W (Table 2). Comparison is given between experimental and numerical simulations when using the heat source parameters deduced by Eq. (13) : $r_{int,2} = 64.6$ µm, $\alpha_{s,2} = 8.98\ \text{mm}^{-1}$ and $\alpha_{l,2} = 3.88\ \text{mm}^{-1}$.

The melt pool width and depth have also been plotted as a function of the linear energy E_l, as shown in Figure 11. The same global tendencies can be observed in both simulations and experimental results. The main differences come from cases $P_L 42 v_L 50$ and $P_L 84 v_L 100$ ($E_l = 0.84\ \text{J} \cdot \text{mm}^{-1}$), for which the numerical simulations showed a shallower melt pool than seen in experiments (see also Figure 10(b)). However, the deviation of melt pool width was higher than that of depth, as indicated by the cases with $E_l = 0.42$ and $0.84\ \text{J} \cdot \text{mm}^{-1}$. Besides the possible higher measurement dispersion in width, this may have been affected by the wetting of lateral powder and possible powder denudation.

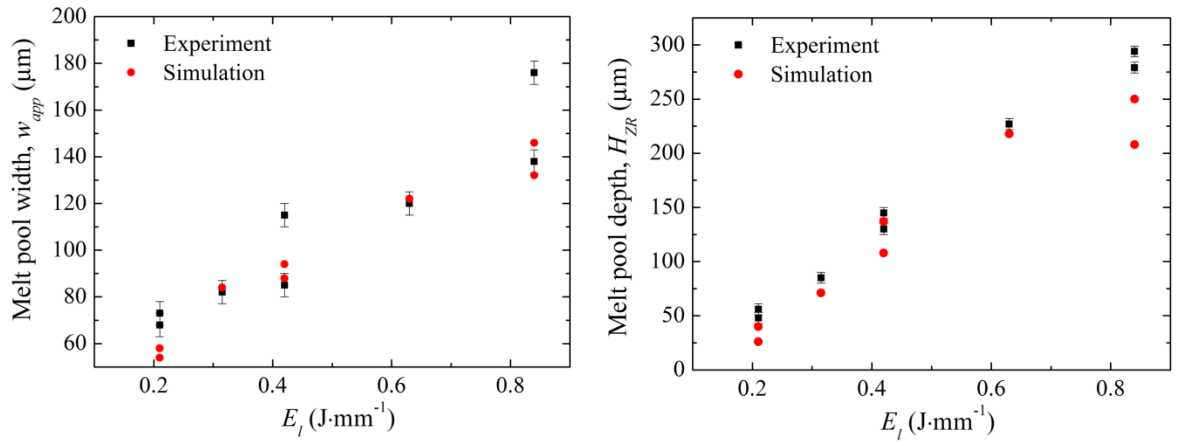

(a) (b)

Figure 11: Melt pool (a) width, w_{app}, and (b) depth, H_{ZR}, as a function of the linear energy, E_l, for all heat source parameters listed in Table 2. Comparison is given between experiments and numerical simulations using $r_{int,2} = 64.6$ µm, $\alpha_{s,2} = 8.98\ \text{mm}^{-1}$ and $\alpha_{l,2} = 3.88\ \text{mm}^{-1}$.

Note that the effective interaction radius r_{int} was about twice as large as the nominal laser radius r_L. This value can be explained by beam scattering and multiple reflections in the powder bed, especially at low linear energies (and high scanning speeds). This is all the more true as the particle material was transparent to the radiation, which also explains the use of a volumetric heat source. It might also be due to the simplicity of the in-depth Beer-Lambert absorption model. Indeed, considering Equation (4), it can be seen that the laser beam (with a surface interaction radius r_{int}) is assumed to propagate vertically in the material (r_{int} being kept the same along the penetration z). A more sophisticated model could be proposed using a diverging conical propagation. Another improvement would require defining two different interaction radii, one for unmelted state (powder bed and solid) and another for the liquid state.

Even though literature values for absorption coefficients are scarce and show a large scatter for Al_2O_3, the identified values are relatively close. The review conducted by Bityukov and Petrov (2013) showed that values vary from 1 mm^{-1} at the melting point to 60 mm^{-1} at boiling point for pure powders, and from 20 mm^{-1} to 90 mm^{-1} for impure powders. The value for the dense material at room temperature reported by Sola and Peña (2013) was 1 mm^{-1}. Identified values obtained for the studied sample ($\alpha_{s,2} = 8.98\ \mathrm{mm}^{-1}$ and $\alpha_{l,2} = 3.88\ \mathrm{mm}^{-1}$) were in the range of values taken from the literature since they were calculated for an "impure" powder deposited on a pure dense substrate. In this case, the carbon added to the powder combusted during melting and changed the optical properties. Note that optical properties are very sensitive to slight changes in chemical composition and porosity of ceramic samples, and available literature does not specify precise properties of the materials.

5. Discussion on results obtained by finite element simulation

5.1. Melt pool sections

Transverse sections of the tracks revealed melted zones when observed by Scanning Electron Microscopy (SEM), as explained in Section 2.2 and Figure 3. Results are displayed in Figure 12, in which melted zones are contoured with blue color for clarity. The melt pool became larger and deeper when the laser power was increased and with decreasing scanning speeds. For cases with a high linear energy (*e.g.* P_L42v_L50 and P_L84v_L100), the melt pool shape appeared like a bolt, with very deep penetration into the substrate. In addition, crack occurrence between substrate and melt pool was more visible than for cases with low linear energy values such as P_L42v_L200 and P_L84v_L400. This was probably caused by higher tensile stresses after complete solidification for higher linear energy values. The experimental results are overlaid with simulated melt pools as red contours. Numerical shapes are in excellent agreement with experiments for medium linear energy such as P_L42v_L100 and P_L84v_L200, and in good agreement for low linear energy (*e.g.* P_L42v_L200). However, for the cases with higher linear energy and deep penetration, *e.g.* P_L42v_L50 and P_L84v_L100, the evolution of sections (width and depth) was different: experimental melt pools have a thinner width along depth, and a greater depth. However, in total, the agreement between calculated and observed melt pool shapes is very good over the whole experimental data base selected for comparison.

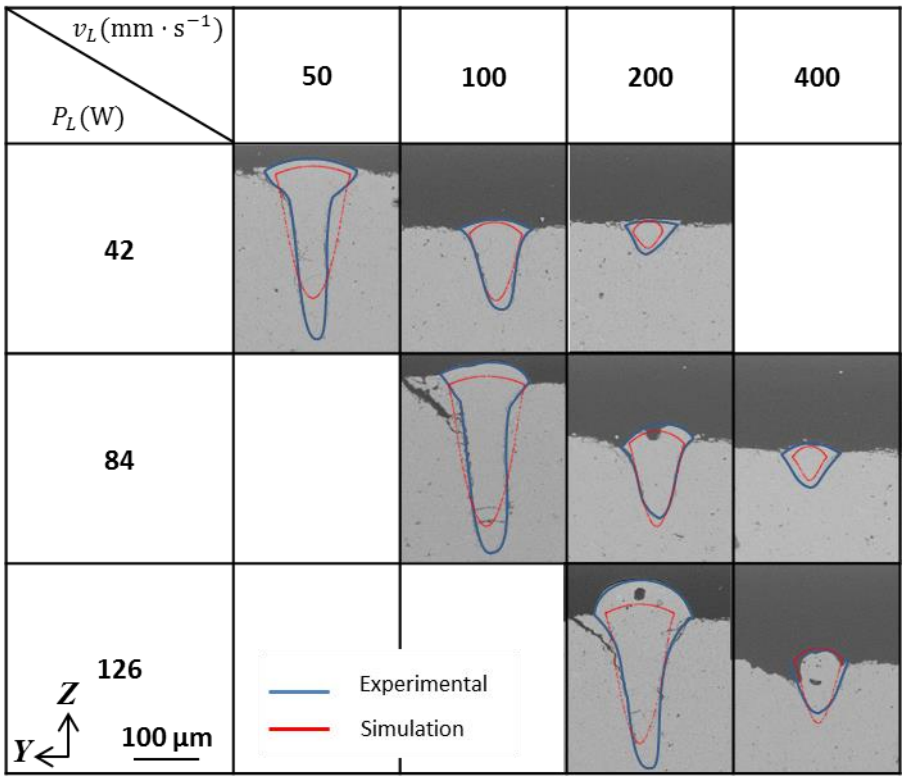

Figure 12: Transverse cross sections of tracks revealing the melt pool shapes under different process conditions (P_L, v_L) highlighted in blue for experimental results and in red for finite element results.

5.2. Track morphology

The prediction of track morphology is difficult as it results from several phenomena, such as surface tension (including the Marangoni effect), evaporation, local powder packing, absorber distribution and even solidification. The present numerical model is based on a continuous description of the powder bed (*i.e.* a continuum) and apparent properties of the materials. Evaporation is neglected and the calculated track shape was expected to be mainly influenced by the hydrodynamics driven by surface tension and solidification. In the melt pool, the resulting Reynolds number can be roughly estimated as about 5.7 (taking $\rho \approx 4000\ \mathrm{kg \cdot m^{-3}}$, maximum velocity $v_{max} \approx 0.5\ \mathrm{m \cdot s^{-1}}$, characteristic size $L \approx 0.1$ mm and liquid viscosity $\mu^a \approx 0.035\ \mathrm{Pa \cdot s}$), meaning that the liquid flow was laminar and thus no

modeling approximation of viscosity was used in the simulation. The track height measured by optical profilometry is compared with two cases associated with low linear energy, $P_L 42 v_L 200$ and $P_L 84 v_L 400$, showing less risk of evaporation. The comparison is shown in Figure 13. The track height profile was taken in the longitudinal median plane. Note that from the non-stationary flow field simulations, only the portion of the tracks between axial coordinates $x = 0.5$ mm and 2.5 mm have been plotted, i.e. sufficiently distant from the start and end of the tracks and thus associated with a quasi-steady state regime. Experimental results clearly showed height variations in the scanning direction. This is also predicted by the numerical simulation as a result of melt pool dynamics.

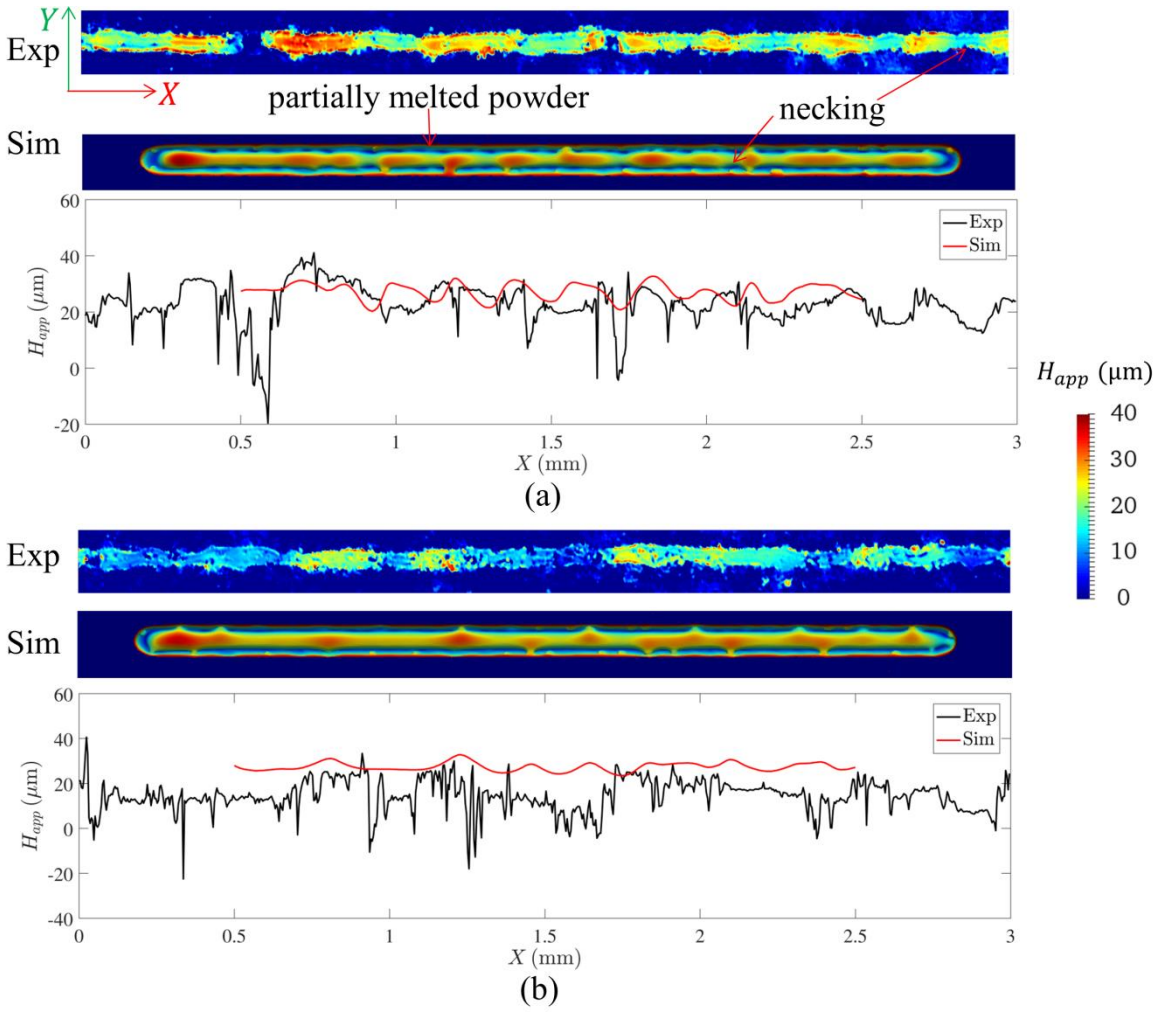

Figure 13: Comparison of (Exp) experimental measurement and (Sim) numerical prediction of the (top view) track height maps and (bottom graph) profiles along the xz median plane for (a) $P_L 42 v_L 200$ and (b) $P_L 84 v_L 400$.

For the case $P_L 42 v_L 200$, the distribution of calculated track heights shows coherence with the experimental results. The width variation was indicated by regions of partially melted powder, also corresponding to abrupt variation of the height. Lateral spikes were present which locally enlarged the area of the track cross section as visible in the simulations. Necking also occurred between spike regions. This phenomenon was the initiation of track interruption and was related to melt pool instabilities. Similar observation can be made on experimental data, through sharp variations of the height. These high frequency variations measured by optical profilometry could also be related to porosities, or liquid spattering, or

more basically the intrinsic granular nature of the powder bed with the presence of particles of different sizes. However, such phenomena have not been considered in the present numerical model. Nevertheless, if such high frequency variations are neglected and low frequency variations, which are supposed to result from fluid dynamics in the melt zone, are considered, simulation matches well with the experimental results for both the average and amplitude variation of the track height.

For the case P_L84v_L400, the average height in experiment was lower than for P_L42v_L200. This clear difference may have been induced by enhanced spattering or more particle ejections at higher scanning speeds, limiting the amount of melted ceramic. The average height of the simulation however remained close to P_L42v_L200 as expected whilst the height variation was smaller and the track appeared to be smoother. Indeed, the melt pool with a smaller section could be more easily perturbed by fluid dynamics, causing more surface fluctuations, leading to discrepancy in track geometry observed in section planes.

Knowing the fine adapted mesh and small time steps used in simulations, there was no chance that the fluid dynamics, leading to surface waviness, could be dramatically affected by numerical instability. The melt pool surface resulted from the coalescence of liquid droplets formed by newly melted powder at the front of the melt pool. However, the surface waviness was mainly due to the effect of surface tension. When this phenomenon was more pronounced, it led to the baling effect presented in the next section.

5.3. Balling effect

In LBM, balling is an important phenomenon of track instability. It results in poor surface quality and mechanical performance as the deposited layer is discontinuous and not well attached to the previously consolidated layer. This happens when the ratio of melt pool length over diameter reaches the Rayleigh-Plateau limit. For a simple case with a cylindrical melt

pool, destabilization of the melt pool into droplets occurs if the length exceeds the circumference (Gusarov et al., 2007). In LBM, such destabilization could be encountered with high scanning speeds and associated with low linear energy. In fact, it can be seen in the tendency for balling in case $P_L 84 v_L 800$ in Figure 1. It is not very clear due to ejection of powder material (denudation), which led to only a few material deposits on the substrate. In order to study the balling effect, additional simulations were carried out and are reported below.

Figure 14(a) shows the progressive appearance of balling with $P_L = 84$ W as predicted by numerical simulation when the scanning speed was increased to different values. With $v_L = 550\ \text{mm} \cdot \text{s}^{-1}$, the track suffered from interruptions, showing the transition from a continuous track to a destabilized track affected by the balling effect. A more pronounced balling effect, with isolated islands, became apparent by a simulation with v_L = 600 mm $\cdot$ s^{-1}. These islands seem to be periodically arranged along the scanning trajectory, except for the fifth, which is connected to its neighbour. When the scanning speed was further increased to 800·mm $\cdot$ s^{-1}, less material was melted and the interrupted track became narrower. It can be noticed that the spacing between isolated islands was smaller than for the case with $v_L = 600\ \text{mm} \cdot \text{s}^{-1}$, the islands being themselves smaller and formed at a higher frequency. In fact, the substrate was still slightly melted with $v_L = 550\ \text{mm} \cdot \text{s}^{-1}$, which it was not when the balling effect appeared in cases with $v_L = 600$ and $800\ \text{mm} \cdot \text{s}^{-1}$, thus forming molten and re-solidified droplets that were not attached to the base material. The non-attachment of the track fragments to the substrate with high v_L may facilitate the ejection of material, explaining the absence of melted powder with $v_L = 800\ \text{mm} \cdot \text{s}^{-1}$ in Figure 1. In Figure 14(b), the height map and profile for the case with $v_L = 600\ \text{mm} \cdot \text{s}^{-1}$ show that the maximum height of islands reaches almost 50 μm, which was close to the initial thickness of the powder bed. In addition, the zones between isolated islands ws at the same level of the initial substrate

surface. This means that the liquid above the substrate was cleaned and gathered in the form of islands under the effect of surface tension.

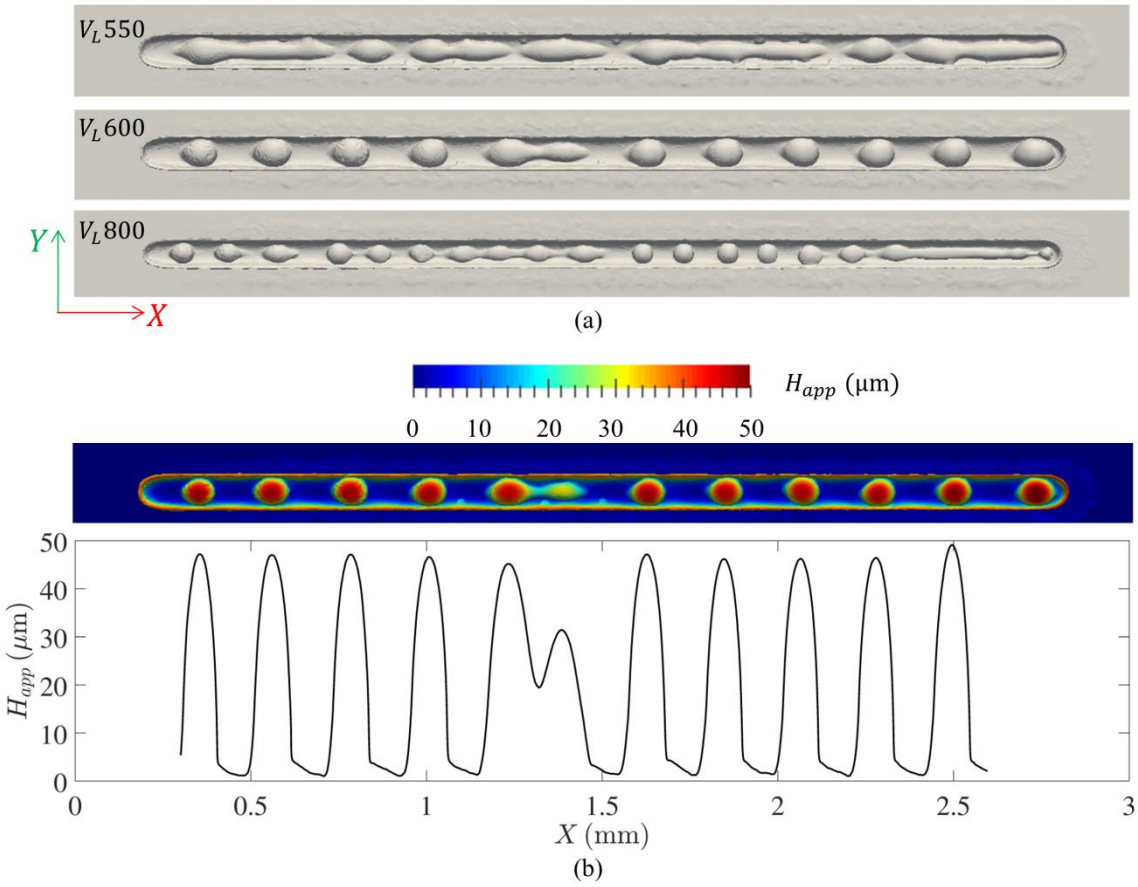

Figure 14: Balling effect illustrated by simulation with a laser power of 84 W with (a) track surface morphology with v_L = 550, 600 and 800 mm · s^{-1}, (b) track height map and track height profile along scanning direction with v_L = 600 mm · s^{-1}.

In order to better understand the formation of isolated track islands, a series of snapshots is shown in Figure 15 for the case P_L84v_L600. At time t = 1 ms, the principal melt pool (the right-hand part) was developing by the fusion of the powder bed. It developed further, at t =1.1 ms, but tended to shrink under the effect of surface tension at 1.11 ms, leading to a neck in the contact region between the liquid and the powder bed. As a lot of energy was accumulated in this small melt pool, because heat extraction by the substrate was limited due

to the small contact area, the maximum temperature at $t = 1.1$ ms rose up to 2896 °C, even higher than the maximum value (~2370 °C) obtained in case P_L84v_L400 with a higher linear energy. Note that this temperature was close to the boiling point (2970 °C), meaning greater risk of evaporation. The neck was then broken at $t = 1.13$ ms. The melt pool retracted in the axial direction due to surface tension, forming the third melt island from the beginning of the simulation. The fusion of powder continued to develop the principal melt pool. This phenomenon was periodic with a distance of about 0.21 mm and a series of islands was left behind the laser. The molten islands solidified and resulted in the final track in the form of a series of islands. An exception occurred for the principal melt pool at t =1.8 ms. It was not totally broken and remained in contact with its neighbour (t =2 ms and 2.3 ms), leaving two solidified islands connected ($t =$ 4.4 ms). Behind the laser, the cooling was uneven as the temperature was higher in the islands than in the regions between them as shown at $t = 4.4$ ms. Consequently, the temperature peaks appeared along the profiles taken at the interface ($\psi = 0$) and just below the initial substrate surface ($z = 0.94$ mm), leading to alternate directions of the temperature gradients, which probably affected the microstructure and stress formation.

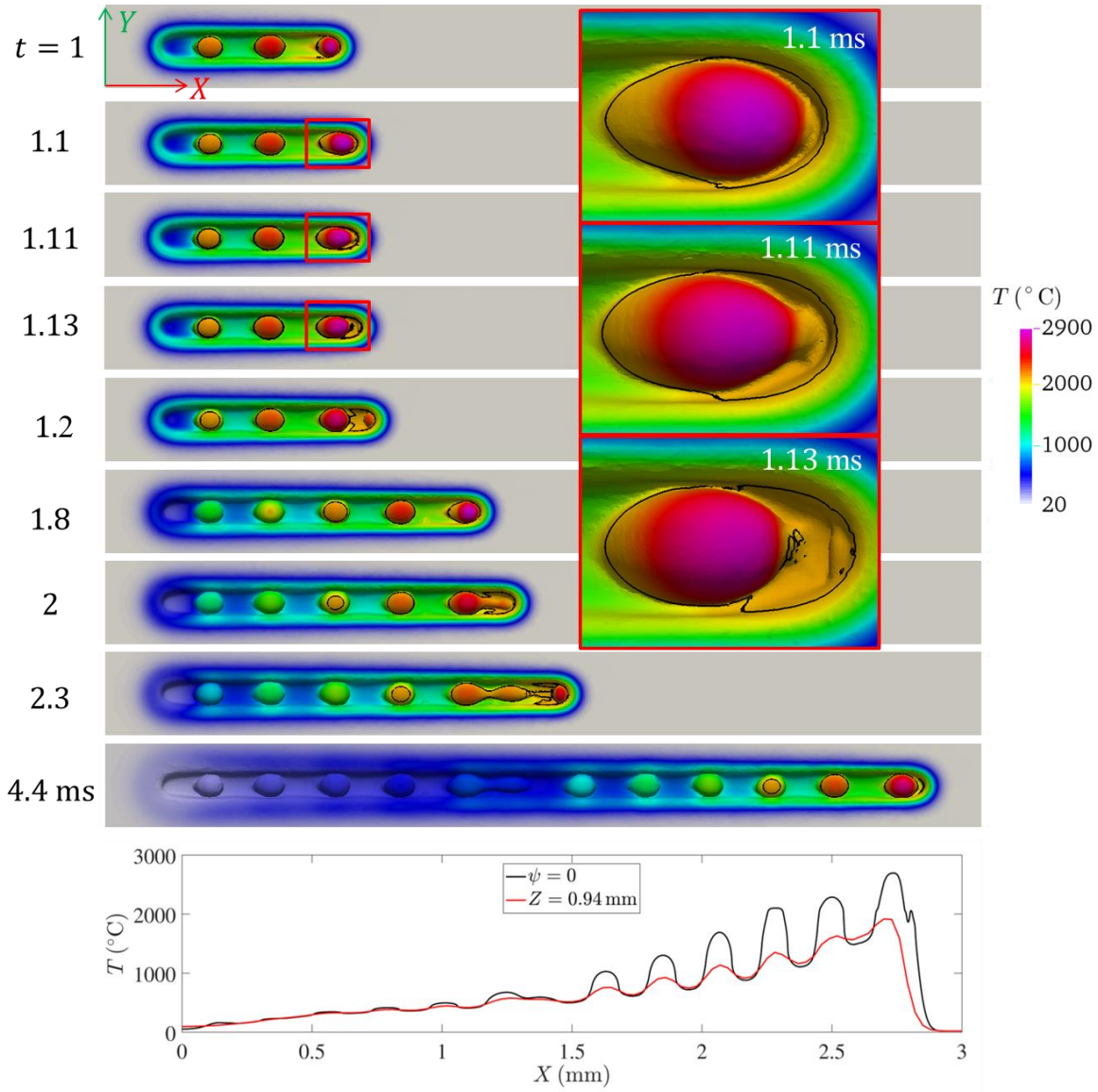

Figure 15: Temperature distribution at different instants for the case $P_L 84 v_L 600$. The black contours correspond to the liquid zones. In the chart at the bottom, two temperature profiles are shown at time $t = 4.4$ ms in the xz median plane. The black profile is at the gas/material interface ($\psi = 0$), while the red one is at $z = 0.94$ mm (9 µm below the initial substrate surface).

6. Conclusions

A comparison between simulations and experiments has been undertaken for LBM of alumina with a Yb:YAG laser. Experiments were carried out for single track melting under different process conditions, leading to various track stabilities and melt pool shapes. Reflectance measurements are reported, pointing out its dependence with the LBM process parameters. A set of process conditions of interest was selected from these experiments corresponding to valuable melting pool dimensions. The parameters defining the volumetric heat source model were the solid and liquid absorption coefficients and the interaction radius of the laser heat source. They were first calibrated with the help of an analytical model. A more sophisticated numerical model has then been applied with the calibrated heat source so as to optimize a second set of parameter values. The simulated melt pool dimensions showed good agreement with experimental measurements with respect to different processing conditions, although some differences were still present at the highest linear energies. The comparison of track stability was more difficult due to the presence of evaporation, liquid spattering and powder denudation, which have not been taken into account in the present model. However, cases with low linear energy can still show similar track height variations. Cases of the balling effect were investigated with high scanning speeds. The formation of interrupted tracks was clearly shown by the numerical model and its influence on temperature distribution illustrated. For future work, a comparison of 2D superimposed track melting with different scanning strategies (including scanning directions and hatch distance) would be interesting to investigate. In addition, the model may be completed by the integration of the recoil pressure induced by evaporation.

Acknowledgements

This work has been conducted within the framework of the CEFALE project, part of the ACLAME program funded by the Institute CARNOT M.I.N.E.S (Paris, France).

References

M. Akita, Y. Uematsu, T. Kakiuchi, M. Nakajima, R. Kawaguchi, 2016. Defect-dominated fatigue behavior in type 630 stainless steel fabricated by selective laser melting, Material Science and Engineering A. 666, 19–26.

I.A. Aksay, J.A. Pask, R.F. Davis, 1979. Densities of $SiO_2 - Al_2O_3$ melts, Journal of American Ceramic Society. 62, 332–336.

M. Ashby, H. Shercliff, D. Cebon, 2013. Matériaux : ingénierie, science, procédé et conception, Presses polytechniques et universitaires romandes.

M. Averyanova, P. Bertrand, B. Verquin, 2011. Manufacture of Co–Cr dental crowns and bridges by selective laser melting technology, Virtual and Physical Prototyping. 6, 179–185.

V.K. Bityukov, V. Petrov, 2013.Absorption coefficient of molten aluminum oxide in semitransparent spectral range, Applied Physics Research. 5, 51-71.

L. R. Carillon. 2007. Étude expérimentale et théorique de l'émission infrarouge de céramiques à haute température. Application aux barrières thermiques. Ph.D. Thesis (in French), Institut National des Sciences Appliquées de Lyon.

M.W. Chase, 1998. Thermochemical tables, NIST-JANAF.

Q. Chen, G. Guillemot, Ch.-A. Gandin, M. Bellet, 2017. Three-dimensional finite element thermomechanical modeling of additive manufacturing by selective laser melting for ceramic materials, Additive Manufacturing. 16, 124–137.

Q. Chen, G. Guillemot, Ch.-A. Gandin, M. Bellet, 2018. Numerical modelling of the impact of energy distribution and Marangoni surface tension on track shape in selective laser melting of ceramic material, Additive Manufacturing. 21, 713-723.

J.A. Dantzig, M. Rappaz, 2009. Solidification, EPFL-Press.

G. Defillon, J.-B. Gueusquin, N. Iooss, 2014. Modèle du bain de fusion de SLM sur céramique avec disparition de l'agent absorbant restreinte au bain. Internal technical report (in French), Mines ParisTech.

P. Fischer, V. Romano, H.P. Weber, N.P. Karapatis, E. Boillat, G. Glardon, 2003. Sintering of commercially pure titanium powder with a Nd:YAG laser source, Acta Materialia. 51,1651–1662

V. Gunenthiram, P. Peyre, M. Schneider, M. Dal, F. Coste, R. Fabbro, 2017. Analysis of laser–melt pool–powder bed interaction during the selective laser melting of a stainless steel. Journal of Laser Applications. 29(2), 022303.

A.V. Gusarov, I. Smurov, 2010. Modeling the interaction of laser radiation with powder bed at selective laser melting, Physics Procedia. 5, 381‑394.

A.V. Gusarov, I. Yadroitsev, Ph. Bertrand, I. Smurov, 2007. Heat transfer modelling and stability analysis of selective laser melting, Applied Surface Science. 254, 975-979.

Y.-C. Hagedorn, J. Wilkes, W. Meiners, K. Wissenbach, R. Poprawe, 2010. Net shape high performance oxide ceramic parts by selective laser melting, Physics Procedia. 5, 587–594.

N.J. Harrison, I. Todd, K. Mumtaz, 2015. Reduction of micro-cracking in nickel supperalloys processed by selective laser melting: a fundamental alloy design approach, Acta Materialia. 94, 59–68.

S.A. Khairallah, A. Anderson, 2014. Mesoscopic simulation model of selective laser melting of stainless steel powder, Journal of Material Processing Technology. 214, 2627–2636.

S.A. Khairallah, A.T. Anderson, A. Rubenchik, W.E. King, 2016. Laser powder-bed fusion additive manufacturing: Physics of complex melt flow and formation mechanisms of pores, spatter, and denudation zones, Acta Materialia. 108, 36–45.

C. Körner, E. Attar, P. Heinl, 2011. Mesoscopic simulation of selective beam melting processes, Journal of Materials Processing Technology. 211, 978–987.

D. Langstaff, M. Gunn, G.N. Greaves, A. Marsing, F. Kargl, 2013. Aerodynamic levitator furnace for measuring thermophysical properties of refractory liquids, Review of Scientific Instrument. 84, 124901.

J. Lawrence, 2004. An analysis of the beam interaction characteristics of selected lasers with an alpha-alumina bioceramics, Optics & Lasers in Engineering. 41,505-514.

J.F. Li, L. Li, F.H. Stott, 2004. A three-dimensional numerical model for a convection-diffusion phase change process during laser melting of ceramic materials, International Journal of Heat and Mass Transfer. 47, 5523-5539.

J.F. Li, L. Li, F.H. Stott, 2004. Comparison of volumetric and surface heating sources in the modeling of laser melting of ceramic materials, International Journal of Heat and Mass Transfer. 47, 1159-1174.

R. Li, J. Liu, Y. Shi, L. Wang, W. Jiang, Balling behavior of stainless steel and nickel powder during selective laser melting process.2012 The International Journal of Advanced Manufacturing Technology. 59, 1025–1035.

Y.J. Liu, S.J. Li, H.L. Wang, W.T. Hou, Y.L. Hao, R. Yang, T.B. Sercombe, L.C. Zhang, 2016. Microstructure, defects and mechanical behavior of beta-type titanium porous structures manufactured by electron beam melting and selective laser melting, Acta Materialia. 113,56–67.

M.J. Matthews, G. Guss, S.A. Khairallah, A.M. Rubenchik, P.J. Depond, W.E. King, 2016. Denudation of metal powder layers in laser powder bed fusion processes, Acta Materialia. 114, 33–42.

L. Moniz, C. Colin, J.-D. Bartout, K. Terki, M.-H. Berger, 2018. Laser Beam Melting of Alumina: Effect of Absorber Additions, JOM. 70, 1–8.

E.O. Olakanmi, R.F. Cochrane, K.W. Dalgarno, 2015. A review on selective laser sintering/melting (SLS/SLM) of aluminum alloy powders: processing, microstructure, and properties, Progress in Material Science. 74, 401–477.

P.-F. Paradis, T. Ishikawa, 2005. Surface tension and viscosity measurements of liquid and undercooled alumina by containerless techniques, The Japan Society of Applied Physics. 44,5082–5085.

H. Schwab, F. Palm, U. Kühn, J. Eckert, 2016. Microstructure, mechanical properties of the near-beta titanium alloy Ti-5553 processed by selective laser melting, Material & Design. 105, 75–80.

D. Sola, J. Peña, 2013. Study of the Wavelength Dependence in Laser Ablation of Advanced Ceramics and Glass-Ceramic Materials in the Nanosecond Range. Materials. 6(11), 5302-5313.

Y.S. Touloukian, R.K. Kirby, R.E. Taylor, T.T.R. Lee, 1984. Thermal expansion - nonmetallic solids, Thermophysical Properties of Matter, 13. 176–177.

J. Trapp, A.M. Rubenchik, G. Guss, M.J. Matthews, 2017. In situ absorptivity measurements of metallic powders during laser powder-bed fusion additive manufacturing, Applied Materials Today. 9, 341‑349.

D. Wang, S. Wu, F. Fu, S. Mai, Y. Yang, Y. Liu, C. Song, 2017. Mechanisms and characteristics of spatter generation in SLM processing and its effect on the properties, Materials & Design. 117,121–130.

P. Yuan, D. Gu, 2015. Molten pool behaviour and its physical mechanism during selective laser melting of TiC/AlSi10Mg nanocomposites: Simulation and experiments, Journal of Physics D: Applied Physics. 48,035303.

“Dry air properties”, accessed 11 July 2017. http://www.engineeringtoolbox.com/dry-air-properties-d_973.html. .